

4-D Flow Control in Porous Scaffolds: Toward a Next Generation of Bioreactors

Khalid Youssef, *Member, IEEE*, Nanette N. Jarenwattananon, Brian J. Archer, Julia Mack, M. Luisa Iruela-Arispe and Louis-S. Bouchard

Abstract—Tissue engineering (TE) approaches that involve seeding cells into pre-determined tissue scaffolds ignore the complex environment where the material properties are spatially inhomogeneous and evolve over time. We present a new approach for controlling mechanical forces inside bioreactors, which enables spatiotemporal control of flow fields in real time. Our adaptive approach offers the flexibility of dialing-in arbitrary shear stress distributions and adjusting flow field patterns in a scaffold over time in response to cell growth without needing to alter scaffold structure. This is achieved with a multi-inlet bioreactor and a control algorithm with learning capabilities to dynamically solve the inverse problem of computing the inlet pressure distribution required over the multiple inlets to obtain a target flow field. The new method constitutes a new platform for studies of cellular responses to mechanical forces in complex environments and opens potentially transformative possibilities for TE.

Index Terms—shear stress, bioreactor, porous scaffold, flow control, tissue engineering

I. INTRODUCTION

REGENERATIVE medicine aims to produce fully functional tissue for implantation, often in an *ex vivo* setting, for purposes of replacing or regenerating organs. A common TE protocol is to seed cells into pre-determined tissue scaffolds, adjust the physical conditions such as flow rate, nutrients and growth factors, and then measure cell response. In recent years, the role of mechanical forces, such as shear stress, has been recognized in the context of regulating proliferation, migration and morphogenesis [1], [2], [3], [4], [5], [6]. Consequently, considerable efforts have been devoted to tailoring shear stress distributions arising from flow fields applied to bioreactors as a means to study the cellular response due to spatial gradients [7], [8], [9], [10], [11]. The state of the art approach involves creating materials with local porosity gradients [12], [13], [14], [15], [8], [9], [16], [17]. While this is suitable for setting initial conditions in a scaffold at the expense of high material complexity, it fails to accommodate the dynamical aspect where different stages of development lead to changes in material properties.

K. Youssef, B.J. Archer and L.-S. Bouchard are with the Department of Bioengineering, University of California, Los Angeles, 410 Westwood Plaza, Los Angeles, CA 90095 USA (e-mail: louis.bouchard@gmail.com)

N.N. Jarenwattananon and L.-S. Bouchard are with the Department of Chemistry and Biochemistry, University of California, Los Angeles, 607 Charles Young Drive East, Los Angeles, CA, 90095 USA

J. Mack and M.L. Iruela-Arispe and with the department of Molecular, Cell and Developmental Biology, University of California, Los Angeles, 615 Charles E. Young Drive South, Los Angeles, CA 90095 USA

L.-S. Bouchard is with the California NanoSystems Institute at UCLA.

L.-S. Bouchard and M.L. Iruela-Arispe are with the Molecular Biology Institute and the Jonsson Comprehensive Cancer Center at UCLA.

It is thus important to develop novel methods that achieve viable growth of thick, immunocompatible tissue. In this article, we present the engineering aspects of a general methodology tailored to spatiotemporally control mechanical forces inside bioreactors. Advantages of our method include the creation of complex flow fields in 3-D environments and the possibility of real-time control in response to cell growth without altering the composition or structure of the scaffold material itself. With the temporal aspect included as the fourth dimension, we refer to the method as 4-D flow control. Our approach can be also used in conjunction with existing methods to enhance their capabilities and add the time component to extend control beyond the initial stages. By adjusting inlet pressures to a multiple-inlet bioreactor we can produce arbitrary flow fields, generating various mechanical force distributions within a single scaffold. Real-time control can be achieved by employing this flow control strategy as part of a feedback control loop that is guided by non-invasive imaging. The spatial distribution of mechanical forces can be altered on demand by dialing-in the appropriate inlet pressure at various inlets, thereby offering flexible means of dynamic control that can adapt to structural changes.

The design and construction of a 10-inlets bioreactor is shown in Fig. 1. The bioreactor is made of non-magnetic material for compatibility with a nuclear magnetic resonance (NMR) environment where maps of fluid velocity inside the reactor are measured [18]. From the flow maps, we calculate the shear rate distributions using finite-difference approximations [19]. This provides an estimate of interstitial flows in the porous scaffold matrix. NMR was selected as the method to assess material properties because of its ability to probe opaque media in a non-invasive manner. Namely, it can be used for investigating the hydrodynamic properties of biomaterials through non-invasive measurements of shear rate, hydraulic pressure and fluid permeability, as demonstrated in recent studies [20], [19].

Our approach operates in two phases, a training phase and an adaptive feedback phase. The first phase involves training a multi-layer perceptron (MLP) to learn the nonlinear relationship between flows applied at the bioreactor's inlets and the shear rate maps resulting in the scaffold. In order to reduce the need for experimental measurements, the MLP is trained with examples obtained from computational fluid dynamics (CFD) simulations that estimate patterns of flow and shear rate based on known material properties, namely fluid permeability and porosity [21], [9]. During this phase, a set of inlet flow speeds is found that can be dialed-in to produce a desired shear rate distribution within a scaffold. The second

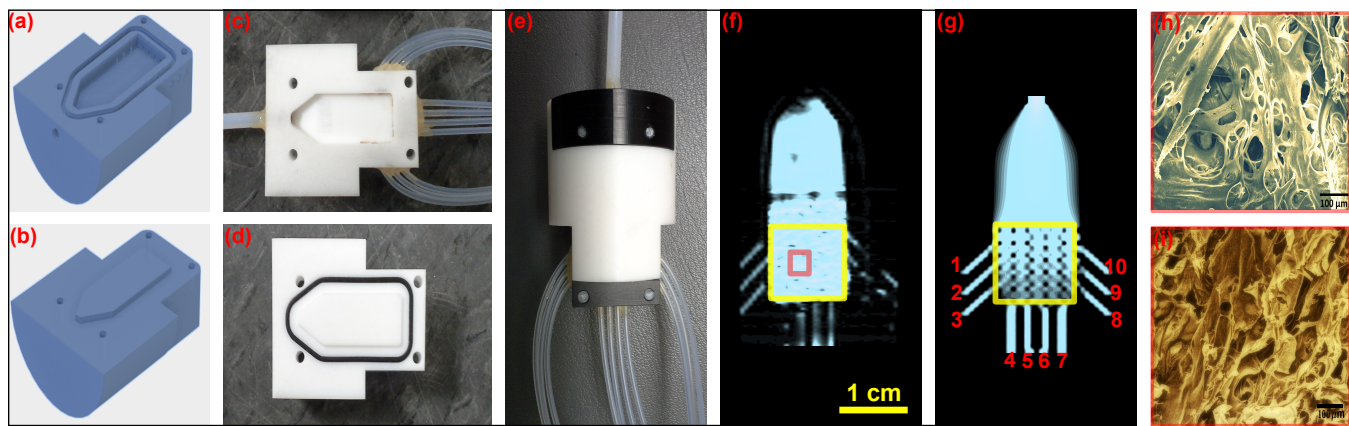


Fig. 1. **Ten-inlet bioreactor.** Design: (a) CAD drawing, bottom part; (b) CAD drawing, top part. Construction: (c) Actual reactor, bottom part; (d) Actual reactor, top part; (e) Fully assembled 10-inlet bioreactor. Fluid region: (f) Proton density NMR image showing the fluid region; (g) Corresponding CFD simulation. The inlets are labeled in (g) for use in Figs. 3, 4, 6, 7 and 9. In (f) and (g) the yellow box indicates the region shown in Figs. 3, 4, 6, 7 and 9. (h) SEM micrograph depicting the pore space of the cellulose scaffold. (i) SEM micrograph depicting the pore space of the collagen scaffold.

phase is where the trained system is applied to adaptively control flow fields in the actual scaffold. Here, non-invasive NMR velocimetry measurements are used to determine flow velocities and shear rate distribution in the scaffold. These measurements can be used to provide feed back for adaptive fine tuning or adjustment of the shear rate maps in the scaffold.

II. MATERIALS AND METHODS

A. 10-channel bioreactor design

A bioreactor featuring ten input channels and one output channel was designed to demonstrate our method, as shown in Fig. 1. Inlets are distributed around a chamber that holds a 3 mm-thick scaffold. There are 3 inlets at a 45° angle on each side, 4 inlets at the bottom and 1 output channel at the top. Figures 1(a) and 1(b) show the CAD drawings of the bioreactor design. Fig. 1(c) and (d) show the actual bioreactor, and Fig. 1(e) shows the fully-assembled bioreactor. The bioreactor and its parts were made of NMR-compatible materials such as PTFE. The bioreactor is designed to fit in a 40 mm-i.d. NMR imaging probe. Inlets are connected to current-controlled mini proportional valves (Kelly Pneumatics, Inc., Costa Mesa, CA). A programmable current regulating circuit was designed to receive commands from a computer program to set the current value at each valve. This enabled computer controlled flow speeds at each inlet.

B. Scaffold

Two different scaffolds were used in these experiments. The first scaffold, a high porosity, high permeability cellulose scaffold was used to demonstrate the ability to generate various flow patterns. No cells were present in this scaffold. The second scaffold was a high porosity, high permeability biocompatible collagen scaffold (Ultrafoam, Central Infusion Alliance 1050020). The collagen scaffold was used for cell experiments to test the biocompatibility of the system and demonstrate the ability to grow cells. Scaffolds were cut into blocks of size $1.25 \times 1.25 \times 0.3 \text{ cm}^3$. In Fig. 1(h), scanning electron microscopy (SEM) micrographs (JEOL JSM-6700)

reveal pore size and morphology of the scaffolds. Prior to SEM, scaffold samples were sputter-coated with a ~5 nm layer of gold to enhance contrast and reduce sample charging. Porosity was calculated to be approximately 90% for the cellulose scaffold and 93% for the collagen scaffold. Porosity was determined by measuring the water volume absorbed by the scaffold, and dividing it by the total volume of the wet scaffold. To accurately determine the volumes, a replica of the bioreactor chamber, i.e. the region that holds the scaffold inside the bioreactor, was created in a plastic block. The weight of the empty chamber with the dry scaffold was measured using a precision balance. The scaffold was then emerged in water and placed in the chamber and the chamber was filled with water to the fullest. The chamber was then closed tight allowing excess water to exit. The weight of the chamber with the wet scaffold inside was measured. Water volume was determined by subtracting the weight of the empty chamber with the dry scaffold from the weight of the full chamber with the wet scaffold inside. The volume of the wet scaffold is the same as the chamber volume, which is easily calculated from the known inner chamber dimensions. This gives a consistent measurement of the effective porosity corresponding to the wet scaffold inside the chamber, where swelling of the scaffold becomes irrelevant.

Fluid permeability of the scaffolds was measured in a fluid permeability flow chamber with a 1 cm diameter cross section area [19]. Scaffolds being measured were cut into discs 10.1 mm in diameter and 5.3 mm thick prior to wetting. Length of the scaffold and diameter were measured with WorkZone Digital Caliper with a range of 0-200 mm. Scaffolds were held in place by two large pore-density filters. Known flow rates were then applied ranging from 5 to 60 mL/min. The static pressures entering and exiting the flow chamber were also measured. The pressure drop across the scaffold was found by subtracting the pressure drop across the chamber without the scaffold from the pressure drop across the chamber with the scaffold. Pressure was measured using Omega DPG8000 pressure gauges. Two units were mounted to the flow path using pipe T connectors, and digital readouts were read from

the device and recorded once the pressure had stabilized. The permeabilities at each flow rate were then averaged to give a final permeability. Using this information, fluid permeability was determined from Darcy's law (1)

$$\kappa = -\frac{\mu L Q}{A \Delta P}, \quad (1)$$

where κ is the fluid permeability, μ is the viscosity, L is the scaffold thickness, Q is the flow rate, A is the surface area, and ΔP is the pressure drop across the scaffold. The calculated permeabilities were $6.13 \times 10^{-7} \text{ cm}^2$ and $2 \times 10^{-11} \text{ cm}^2$ for the cellulose and collagen scaffolds, respectively.

C. Adaptive control algorithm

Machine learning methods including artificial neural networks are now commonly used to solve a variety of problems in cell biology [22], [23]. We present a novel multiple-input, multiple-output (MIMO) adaptive intelligent control algorithm based on MLP. Our algorithm consists of a fast search method designed to guide a MLP to perform an initial estimation of required inlet speeds using CFD simulations, by learning the nonlinear relationship between inlet flow speeds and target parameters. The scaffold was treated as a grid with nine equal regions. The algorithm was configured to create shear rate patterns by simultaneously controlling shear rate mean values in these regions. Thus, the problem in our case involves ten inlets and nine parameters. Parameter values can be adjusted depending on the application requirements. For example, while a 3×3 grid is sufficient in our case for demonstration purposes, higher resolution can be achieved with more computational time. In other applications, the grid can also be concentrated on one small local region rather than the entire scaffold.

The working principle of the algorithm is illustrated in Fig. 2(d). The pseudocode is provided in Algorithm 1 whereas its parameters are listed in Table I. The search algorithm starts with a target shear rate map specified by the user. Mean values from different regions of the map are fed to a MLP as its input, and the output produced by the MLP is used to determine the flow speeds of all ten inlets required to reproduce the desired target map as closely as possible. A new shear rate map corresponding to the inlets' flow speeds generated by the MLP with D inputs is obtained (O_j) and compared to the desired target (T_j) pattern using the cost function ξ_1 of Eq. (2),

$$(\xi_1)^2 = \sum_{j=1}^D \left(\frac{T_j - T_j e^{-\frac{(O_j - T_j)^2}{2d^2}}}{T_j} \right)^2 = \sum_{j=1}^D \left(1 - e^{-\frac{(O_j - T_j)^2}{2d^2}} \right)^2 \quad (2)$$

In principle one could employ a cost function that simply measures the Euclidean distance between a given vector and a target vector, as in Eq. (3),

$$(\xi_2)^2 = \sum_{j=1}^D (O_j - T_j)^2. \quad (3)$$

However, including a Gaussian membership function, as was the case in Eq. (2) can relax the measurement constraints by allowing a small margin of error where an approximate

measurement is considered acceptable. d determines the width of the Gaussian function. Using a d value close to the average target value "smoothes" the error space, which leads to faster convergence. To prevent the search algorithm from biasing towards relatively large target vector components, a normalization is performed by dividing by the target vector, as shown in Eq. (2).

For example, a target shear rate map can have high variations in shear rate values between different regions. Regions with relatively high shear rate values will carry more weight in the cost function. This can cause the obtained solution to be less accurate in regions with relatively low shear rate values. Normalizing as in Eq. (2) allows each region to contribute an equal weight to the cost function regardless of the target value in that region. When the values of O_j and T_j are close to each other, the Gaussian function yields a value close to one, and the contribution of the corresponding measurement to the cost function is small. When the values of O_j and T_j are far apart, the Gaussian function yields a value close to zero, and the contribution to the cost function is large. O_j denotes a measurement (observed value) whereas T_j denotes the corresponding desired measurement (target value). By measurement, we refer to a mean shear rate value associated with one of the scaffold regions.

The initial MLP output does not yield the most accurate solution. The search algorithm aims to find a solution that is better than the one provided by the MLP, by following a number of rules to introduce changes to the MLP output as shown in the pseudocode below (see Algorithm 1). The new solution is used to update the MLP weights as explained in the following section. This guides the MLP to gradually learn the relationship between the inlets' flow speeds and the target map after a number of iterations. The algorithm was validated by applying it to a 2-input control problem where the convergence path through the error space can be visualized on a 3-D plot. Results from the validation are shown in Fig. 2(a-c).

D. Solution by multi-layer perceptron

Multi-layer perceptrons have been shown to be universal function approximators [24]. A MLP with D inputs, K outputs, one hidden layer with M nodes yields a K -dimensional output vector \vec{y}_t whose k -th component is given by iterated hyperbolic tangents:

$$\tilde{y}_t(k) = \tanh \left(\sum_{l=0}^M \theta_{l,k}^{(2)} \tanh \left(\sum_{j=0}^D \theta_{j,l}^{(1)} x_t(j) \right) \right), \quad (4)$$

where

$$z(l) = \tanh \left(\sum_{j=0}^D \theta_{j,l}^{(1)} x_t(j) \right), \quad (5)$$

and for which $l = 0, \dots, M$ are the outputs of the hidden layer. We use the convention where $x_t(0) = 1$ and $z(0) = 1$, so that $\theta_{0,l}^{(1)}$ and $\theta_{0,k}^{(2)}$ represent biases to the transfer function.

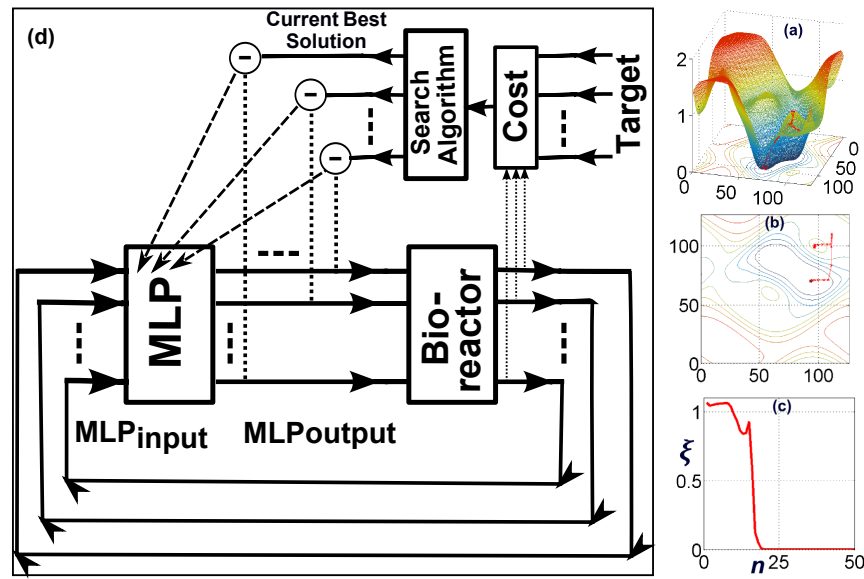


Fig. 2. (a-c) Two-input control validation results. The convergence path shows the search starts at a maximum, avoids getting stuck in a local minimum and finds its way to a global minimum in a small number of steps. (a) 3-D plot of the error space. (b) 2-D contour projection of the error space. (c) Convergence plot with y -axis corresponding to the cost function and x -axis corresponding to the iteration number. (d) System design of the control algorithm. A MLP block gets its inputs from shear map measurements of the scaffold inside the bioreactor, and produces outputs to update inlets' flow speeds such that the shear rate map in the scaffold is closer to the target shear rate map. The MLP training is guided by the search algorithm that evaluates the MLP performance using the cost function evaluation block (Cost), and determines the training samples presented to the MLP.

TABLE I
LIST OF THE ALGORITHM'S MAIN PARAMETERS.

Parameter	Description	Range	Used Value
μ	Learning rate	$\mu_{min}:\mu_{max}$	Automated
a	Momentum	$a_{min}:a_{max}$	Automated
μ_{min}	μ lower bound	>0	1.00E-06
μ_{max}	μ upper bound	$>\mu_{min}$	5.00E-02
a_{min}	a lower bound	>0	1.00E-06
a_{max}	a upper bound	$>a_{min}$	5.00E-02
dso	Search step size multiplier	>0	5.00E-01
ds	Search step size: $\xi \cdot dso$	>0	Automated
ξ	Cost function value	NA	Automated
D	Number of MLP inputs	>0	9
K	Number of MLP outputs	>0	10
boutput	MLP output with current minimum cost	NA	NA
ξ_b	Current best cost value	NA	NA
bcount	Maximum MLP training epochs for current best output	>0	3
d	membership function dilatation parameter	>0	3

The generalization to arbitrary numbers of hidden layers is straightforward by nesting additional hyperbolic tangents. The calculation of the vector \vec{y} is called feed forward propagation.

A MLP with nine inputs corresponding to the nine scaffold regions, and ten outputs corresponding to the ten channels is used. Mean values from nine regions of the shear rate map are stored in a vector denoted by \vec{x}_i and used as inputs to a MLP whose transfer function is a hyperbolic tangent, has ten outputs corresponding to the ten inlets of the bioreactor, and includes two hidden layers with ten nodes each. The Back-Propagation with Adaptive Learning rate and Momentum term (BPALM) method [25] was used to update the MLP

weights. This technique is suitable in our case since the MLP is trained online one target vector at a time, and since it offers convergence acceleration as compared to the original back propagation method proposed by [26] by introducing an adaptive learning rate and momentum term.

E. CFD shear rate simulation.

Many complex models of porous media have emerged due to advances in the field of CFD. However, they require a detailed characterization of the effective-medium properties of the scaffold in terms of the microscopic properties and remain computationally expensive. Hundreds of simulations

Algorithm 1 Control Algorithm pseudo-code

```

1: Initiate MLP inputs
2: Evaluate shear stress map for MLP outputs
3: Compare to target
4:  $\xi_b \leftarrow \xi$ 
5:  $\xi_1 \leftarrow \xi$ 
6:  $count = 0$ 
7: Reset
8:  $flag = 0$ 
9: Reset input picking
10: Pick
11: Randomly pick one of the inputs
12: Increase its speed by  $ds$ 
13: Evaluate shear stress map for resulting input
14: if  $\xi > \xi_b$  then
15:   Decrease its speed by  $ds$ 
16:   Evaluate shear stress map for resulting input
17:   if  $\xi > \xi_b$  then
18:     goto Check
19:   else
20:     goto update
21: else
22: update
23:    $\xi_b \leftarrow \xi$ 
24:    $count = 0$ 
25:   Update MLP
26:    $flag = 1$ 
27: Check
28:   if All inputs picked then
29:     if  $flag = 1$  then
30:       goto Reset
31:     else
32:        $count = count + 1$ 
33:       if  $count > bcount$  then
34:          $\xi_b \leftarrow \xi$ 
35:          $count = 0$ 
36:         Update MLP
37:         goto Reset
38:       else
39:         Perturb
40:         Add random vector multiple of  $ds$  to input
41:         Evaluate shear stress map for resulting input
42:         if  $\xi > \xi_b$  then
43:           goto Perturb
44:         else
45:            $\xi_b \leftarrow \xi$ 
46:            $count = 0$ 
47:           Update MLP
48:           goto Reset
49:         else
50:           goto Pick

```

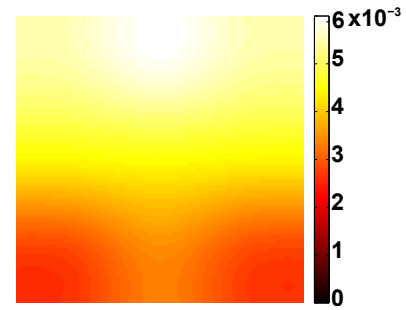


Fig. 3. **Map of local Reynolds numbers.** Measured across the scaffold region under conditions of maximum flow rate at each input of the scaffold. This region corresponds to the region highlighted by the yellow square in Fig.1(f) of the main text. The average Reynolds number is on the order $\sim 10^{-3}$.

are required during the training phase, typically in the range of the number of inputs multiplied by the number of iterations. Consequently, we opted for a simple laminar flow model as an approximation of the complex medium. While the laminar flow model is not recommended for modeling porous media in general, it is used here to save computational time. The porous media was modeled as a distribution of circular obstacles as shown in Fig. 1(g), where the porosity and permeability were chosen similar to the scaffold. This approximation is justified by Reynolds numbers calculation throughout the model using (6) when the maximum flow rate is applied to all channels at once, where they are consistently much less than 1 in the investigated flow range as shown in Fig. 3. Variations from the more accurate and computationally expensive methods that explicitly model the geometry of the microscopic pore space are minimal. Due to the adaptability of the control algorithm, as demonstrated in Fig. 5(d,e,f) and Fig. 6 (details in the Results section), any inaccuracies produced by the approximation can be compensated for in the second phase where simulations are replaced with real NMR measurements.

$$ReCell(x, y) = \frac{h\rho\sqrt{v_x^2(x, y) + v_y^2(x, y)}}{4\mu} \quad (6)$$

$ReCell$ is the Reynolds number value for a cell in the mesh, h is the average mesh size (along x or y), ρ is the fluid density, $v_x(x, y)$ and $v_y(x, y)$ are the velocity components at the point (x, y) , and μ is the viscosity.

Finite element analysis software COMSOL Multiphysics (COMSOL Inc., Burlington, MA) was used to solve the Navier-Stokes equations for incompressible Newtonian laminar flow with no slip boundary conditions:

$$\begin{aligned} \rho(U \cdot \nabla)U &= \nabla \cdot [-P + \nu(\nabla U + \nabla U^T)] - \rho G, \quad (7) \\ \rho \nabla \cdot U &= 0, \quad U = 0 \text{ at walls.} \end{aligned}$$

U denotes the velocity vector field ($m \cdot s^{-1}$), P is the pressure (Pa), ρ is density ($kg \cdot m^{-3}$) and ν is the dynamic viscosity ($Pa \cdot s$). The term $\rho \cdot G$ takes gravity into consideration, where G is the gravitational acceleration ($m \cdot s^{-2}$). At the inlets, we set $U = U_{in}$ according to the input speed determined by the algorithm. No viscous stress ($P = P_0$) boundary condition

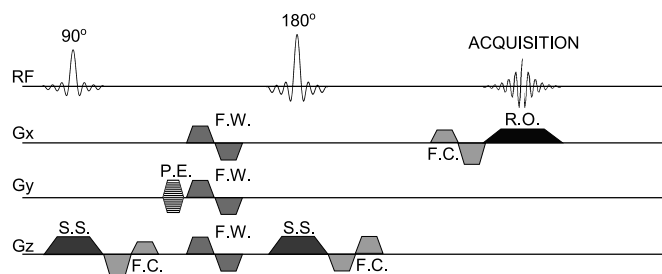


Fig. 4. **Timing diagram of NMR pulse sequence used for flow imaging.** Slice-selective (S.S.) three-dimensional phase-contrast velocimetry 2-D images are generated by repeating the sequence n times while stepping the phase-encode (P.E.) gradient through the phase-encoding scheme. Bipolar trapezoidal flow-weighting (F.W.) gradients were added along the x , y , and z directions to select the gradient first moment (M_1). Flow-compensation (F.C.) gradients are added along x and z directions. Additional abbreviations: S.S. slice select gradient; R.O. read out (frequency encode) gradient.

was selected at the outlet. The velocity field is obtained by solving the Navier-Stokes equation. Shear rate ζ (s^{-1}) is then calculated as a function of the velocity field using finite difference approximations of $\zeta = (\nabla U + \nabla U^T)/2$. Shear stress τ (Pa) is obtained by multiplying shear rate values with the dynamic viscosity, i.e. $\tau = \nu\zeta$.

F. NMR shear rate measurement.

The pulse sequence for the NMR imaging experiment is shown in Fig. 4. A standard spin-echo imaging experiment with slice-select (S.S.), readout (R.O.), and phase-encode (P.E.) gradients was modified to include phase-contrast velocimetry as in refs. [20], [19]. To generate 2-D images, the sequence is repeated n times while looping of the P.E. gradient. Flow-compensation (F.C.) gradients were added along all directions except the P.E. direction. Bipolar, trapezoidal flow-weighting (F.W.) gradients are added along the x , y , and z directions in order to select the gradient first moment M_1 . In the case of no flow, stationary nuclear spins experience the positive and negative lobes of the bipolar F.W. gradient with the same magnitude. For stationary spins, the phase accumulation from the positive lobe is equal and opposite to the phase accumulation from the negative lobe, resulting in zero net phase accumulation. For moving spins, phase cancellation is incomplete [18] and the residual phase accumulation is proportional to velocity. Once we have a velocity map acquired, the corresponding shear rate map can be calculated by taking gradients of the velocity field, as described in the previous section; see also [19]. In this work, velocity measurements represent velocities averaged along the z direction. Shear rate patterns were controlled along the x and y directions.

III. RESULTS

To demonstrate the method's ability to generate complex patterns, several different shear-rate maps were produced sequentially. Two examples of spatial patterns are shown in Fig. 5. Fig. 5(a) shows a non-trivial pattern whereas Fig. 5(d) shows a uniform pattern. CFD simulations of flows within the scaffold of the bioreactor were performed and the results

are shown Fig. 5. The first simulation [see Fig. 5(a-c)] was used to test the algorithm's ability to find inlet flow speeds in the case of a complex shear rate distribution. The pattern consists of a non-linear gradient featuring low shear rates in the lower right hand corner juxtaposed against a high shear rate region located in the upper left hand corner [see Fig. 5(a,b)]. Along the path connecting these two corners, the shear rate values range from $0 s^{-1}$ to $6 s^{-1}$. The convergence plot [see Fig. 5(c)] demonstrates that the algorithm converged to a reasonable solution in less than 25 iterations, and found an accurate solution in less than 50 iterations.

The second simulation Fig. 5(d-f) was designed to test the algorithm's ability to adapt to changes over time. The algorithm was required to find inlet flow speeds to generate a uniform shear rate distribution (shown in Fig. 5(d)). The target shear rate value was originally set to $10 s^{-1}$. After the algorithm converged to a solution for the $10 s^{-1}$ value, the algorithm was kept running until it reached 100 iterations. At that point, the target shear rate value was changed to $11 s^{-1}$ and the convergence speed to the new value was assessed. The convergence plot [see Fig. 5(f)] shows that the algorithm quickly adapts to the new value [see Fig. 5(e)], where only a small number of iterations were required to find a new solution. Note that this ability to quickly adapt to changes allows using crude approximations in training to reduce computational requirements. Additionally, this simulation also illustrates the algorithm's ability to generate a highly uniform shear rate distribution. It is generally difficult to create a uniform shear rate distribution in a bioreactor with only a single inlet; but with ten inlets excellent results could be obtained. Shear rate values in the scaffold varied between $10 s^{-1}$ and $12 s^{-1}$, when the target value selected was $11 s^{-1}$.

In order to assess the algorithm's performance in a dynamic environment where scaffold properties are changing over time, an experiment was conducted where the algorithm was trained to achieve a target shear rate map for the case where a grid of circular obstacles with a $12.5 \mu m$ radius is present. The obstacle radius was then gradually increased to $22.5 \mu m$. The response was assessed by observing the cost function values at the iterations where the radius is increased, and the current shear rate map before the change takes place. This is illustrated in Fig. 6. The results confirm the algorithm's excellent adaptive abilities. Spikes in cost function values corresponding to instances where structural change occurs are characterized by small amplitudes and widths. The small amplitudes indicate the flexibility of the bioreactor design, where structural changes do not cause drastic changes in the shear rate map. The small widths correspond to the small number of iterations required by the algorithm to adapt and readjust the shear rate map back to the desired target after it had converged in its training phase. These results also validate the use of a simplified CFD model in the training phase, in order to reduce computational cost and training time.

Bioreactor biocompatibility was demonstrated by culturing human aortic endothelial cells (HAECs) in endothelial cell growth media (EGM-2 BulletKit, Lonza CC-3162) flowing at $4 mL/min$ total flow distributed uniformly at each individual inlet. Two identical scaffolds were seeded with 2.2×10^6 cells

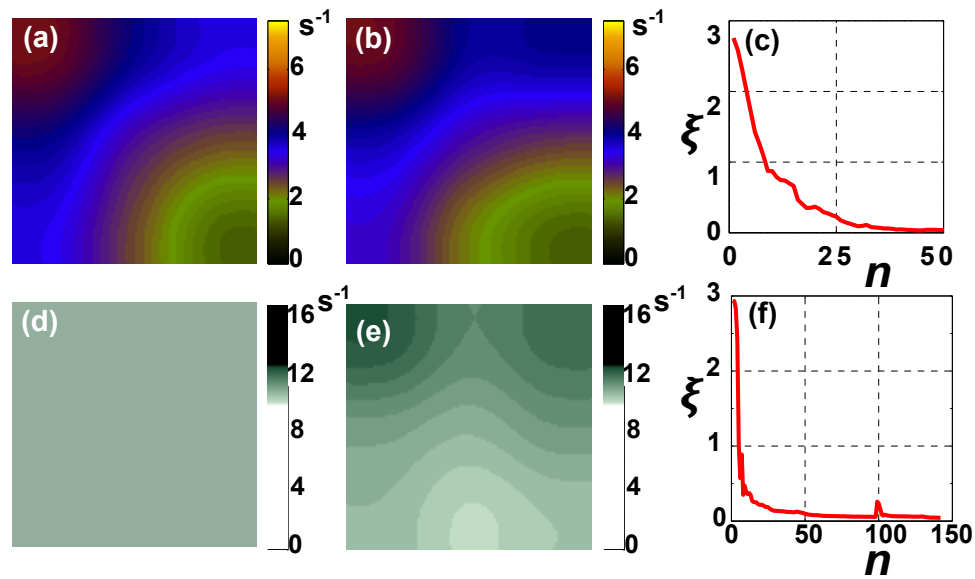


Fig. 5. **Inverse problem solved by multi-layer perceptron.** Results from CFD simulations are shown: (a) Desired target shear pattern; (b) Outcome of applying input flow speeds calculated to generate the pattern shown in (a), rounded to the nearest 0.05 mm/s from inlet #1 to inlet #10 are: [0.50, 0.45, 0.40, 0.15, 0.30, 0.40, 0.80, 1.40, 0.60, 1.20] mm/s, respectively; (c) Convergence plot with the y -axis corresponding to the cost function and x -axis corresponding to iteration number; (d) Uniform shear rate pattern at 11 s^{-1} ; (e) Outcome of applying input flow speeds calculated by algorithm to generate the pattern shown in (d), rounded to the nearest 0.05 mm/s from inlet #1 to inlet #10 were: [0.00, 0.05, 1.70, 1.95, 3.90, 2.75, 3.50, 0.05, 1.20, 0.00] mm/s, respectively; (f) Convergence plot with y -axis corresponding to the cost function and x -axis corresponding to the iteration number.

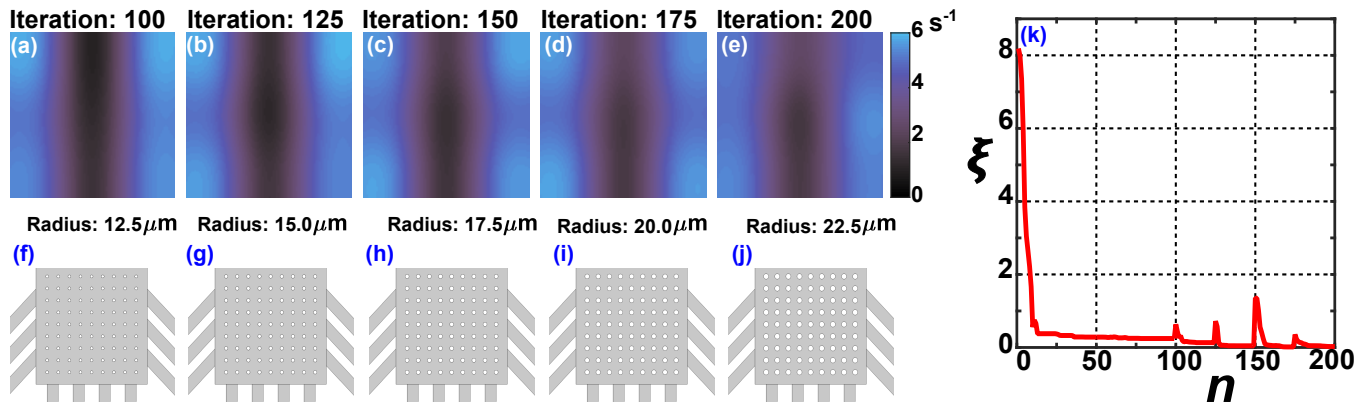


Fig. 6. **Algorithm response to structural changes.** The system was trained to produce the target shear rate map shown in (a) for the case where circular obstacles shown in (f) are present. After 100 iterations the obstacle size was gradually increased every 25 iterations as shown in (g)-(j), and the corresponding shear rate maps are shown in (b)-(e). (k) shows the cost function value (y -axis) at each iteration (x -axis), where spikes at iterations 101, 126, 151, and 176 correspond to the instances where structural change occurs.

and cultured statically at $37 \text{ }^\circ\text{C}$ and 5% CO_2 for 48 hours to promote cell attachment to the scaffold. One scaffold was then transferred to the bioreactor while the other remained static in a tissue culture dish for control. Growth media flowing into the bioreactor was warmed to $37 \text{ }^\circ\text{C}$ and sparged with a 5% CO_2 gas mixture. The scaffolds were cultured for an additional 48 hours in their respective conditions before being fixed in a solution containing 2% paraformaldehyde (PFA). Following fixation the cells were stained for cell nuclei (DAPI) and cytoskeleton (F-actin with phalloidin). Scaffolds were then imaged with a confocal microscope with $15 \text{ } \mu\text{m}$ thick image sections. Imaging results show that cells cultured in the bioreactor survived and proliferated. There were also more cells in the scaffold cultured in the bioreactor compared to static culturing, as evidenced by the number of blue nuclei

as well as associated red F-actin staining. Imaging results are presented in Fig. 7. The shear rate map in the collagen scaffold corresponding to the flow rate conditions under which cells were cultured is shown in Fig. 8. This flow pattern was also used with the cellulose scaffold (Fig. 9a,b).

Using our method, spatial distributions of shear rate values within the scaffold region can be altered over time to generate arbitrary patterns by merely changing inlet flow speeds. The 10-inlet bioreactor's ability to dynamically generate versatile and complex mechanical force distributions within a scaffold is demonstrated in Fig. 9. Three different complex shear rate distributions generated sequentially within the same scaffold are shown. To evaluate the effectiveness of the approximations made in training with our CFD model, maps obtained using initial values obtained from simulations are compared with

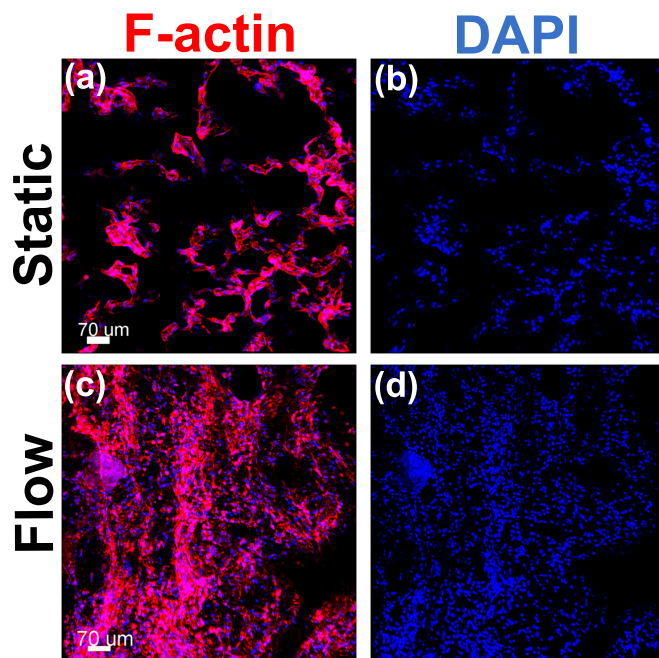


Fig. 7. **Biocompatibility test (collagen scaffold).** (a) & (b) Cell growth under static condition. (c) & (d) Cell growth under flow. (a) & (c) Imaging results for cell nuclei stain (DAPI). (b) & (d) Imaging results for cell cytoskeleton (F-actin with phalloidin).

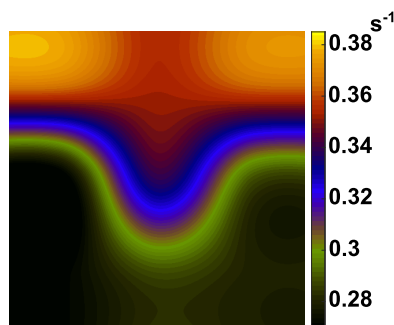


Fig. 8. **Shear rate map in collagen scaffold.** The shear rate map corresponding to the flow under which cells were cultured in the collagen scaffold was obtained using NMR velocimetry.

corresponding shear rate maps as measured experimentally using the NMR velocimetry technique [18], [20], [19]. We observe excellent agreement in the generated patterns between theory and experiments. Using NMR feedback, the algorithm can easily adapt to fine tune the moderate range variations due to the adaptive properties demonstrated earlier in Fig. 5(d-f) and Fig. 6.

IV. DISCUSSION

Tissue engineering studies of the effects of shear flows have been hampered by the lack of suitable platforms to control flow fields. Previous attempts at controlling mechanical forces were limited to altering the scaffold structure and bioreactor geometry. Most bioreactors used to date have been designed to operate with a single inlet. Parameters such as perfusion rate, flow, and mechanical stress are typically selected by trial-and-error. Even then, due to many sources of variability, a protocol

that works to bring a particular construct to a desired stage may likely fail to work for another construct [27]. Thus, the importance of adaptive control with feedback. Given a feedback mechanism, many possible solutions, e.g., single parameter control, or a proportional-integral-derivative controller, may exist for a single-inlet bioreactor. However, a single inlet does not permit fine tuning of the flow field at the microscale, which is an essential element for the study of cellular responses to flow. Bioreactors with multiple inlets, such as the one presented herein, reduce the need for engineering the scaffold material properties, may alleviate manufacturing complexity while enabling the creation of more accurate and complex flow fields. Spatiotemporal control of mechanical force distributions in scaffolds can be used to dynamically control the bioreactor for applications in TE.

Because the relationship between shear maps and inlet pressure is highly nonlinear, the task of finding a set of inlet pressures to generate a desired flow pattern in a 10-inlets bioreactor is a complex adaptive control problem possessing no known analytical solutions. The adaptive control algorithm presented herein solve the problem numerically. The algorithm demonstrates high efficiency, as it converges to a solution with a small number of iterations. Furthermore, it can learn complex input/output relationships between inlet flow speeds and mechanical force distributions, which gives it the ability to quickly adapt to changes.

V. CONCLUSION

The concepts presented here are general and could be applied to controlling any other force field, or the flow of substances (e.g., nutrients, gases). Although not demonstrated here, scaffold structure, bioreactor geometry and inlet positions can easily be included as additional parameters to be optimized along with inlet speeds. An interesting open question would be to verify what shear rate distributions lead to tissue development in a bioreactor scaffold beyond initial stages of cell growth. A possible extension of this work to provide additional control of the flow patterns would be to add multiple outlets to the bioreactor; outlets add more degrees of freedom to the problem where pressure can be released locally.

ACKNOWLEDGMENT

Funding support from the Arnold and Mabel Beckman Foundation and the National Institutes of Health (NIH) award 5 R01 HL114086-03 is acknowledged. Brian Archer was supported by a Ruth L. Kirschstein National Research Service Award T32HL69766 (NIH).

REFERENCES

- [1] A. Engler, S. Sen, H. Sweeney, and D. Discher, "Matrix elasticity directs stem cell lineage specification," *Cell*, vol. 126, no. 4, pp. 677–89, Aug 2006.
- [2] J. Rutkowski and M. Swartz, "A driving force for change: interstitial flow as a morphoregulator," *Trends in Cell Biology*, vol. 17, no. 1, pp. 44–50, Jan 2007.
- [3] K. Saha, A. Keung, E. Irwin, Y. Li, L. Little, and D. Schaffer, "Substrate modulus directs neural stem cell behavior," *Biophysical Journal*, vol. 95, no. 9, pp. 4426–4438, Nov 2008.

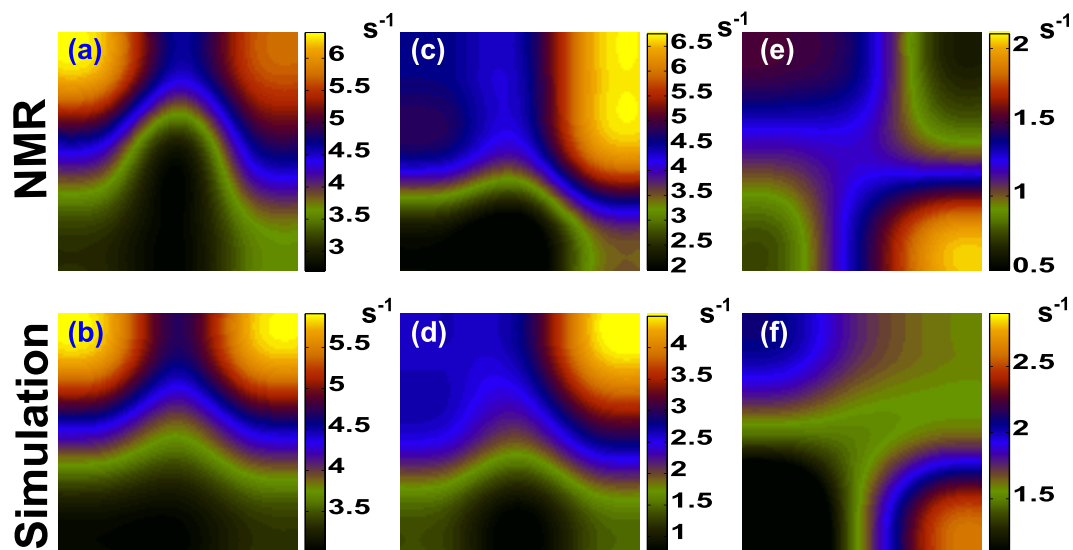


Fig. 9. **Arbitrary shear rate patterns in the same scaffold.** Results from NMR velocimetry in cellulose sponge (a) and CFD simulation (b) for the case where all inlets have same flow speed of 1 mm/s. (c) & (d) are NMR and CFD simulation results, respectively, where inlets [3, 8, 9 & 10] have a flow speed of 1.5 mm/s, and inlets [1, 2, 4, 5, 6 & 7] have zero flow speed. (e) & (f) are NMR and CFD simulation results, respectively, where inlets [4, 5, 8, 9 & 10] have zero flow speed, inlets [6 & 7] have a flow speed of 1 mm/s, and inlets [1, 2 & 3] have a flow speed of 0.5 mm/s.

[4] Z. Syedain, J. Weinberg, and R. Tranquillo, "Cyclic distension of fibrin-based tissue constructs: Evidence of adaptation during growth of engineered connective tissue," *Proceedings of the National Academy of Sciences USA*, vol. 105, no. 18, p. 6537, May 2008.

[5] D. Fletcher and R. Mullins, "Cell mechanics and the cytoskeleton," *Nature*, vol. 463, pp. 485–492, Jan 2010.

[6] R. Udan, T. Vadakkan, and M. Dickinson, "Dynamic responses of endothelial cells to changes in blood flow during vascular remodeling of the mouse yolk sac," *Development*, vol. 140, no. 19, pp. 4041–4050, Oct 2013.

[7] A. Yeatts and J. Fisher, "Bone tissue engineering bioreactors: dynamic culture and the influence of shear stress," *Bone*, vol. 48, no. 2, pp. 171–181, Feb 2011.

[8] F. Melchels, B. Tonnarelli, A. Olivares, I. Martin, D. Lacroix, J. Feijen, D. Wendt, and D. Grijpma, "The influence of the scaffold design on the distribution of adhering cells after perfusion cell seeding," *Biomaterials*, vol. 32, no. 11, pp. 2878–2884, Apr 2011.

[9] A. Lesman, Y. Blinder, and S. Levenberg, "Modeling of flow-induced shear stress applied on 3d cellular scaffolds: Implications for vascular tissue engineering," *Biotechnology and Bioengineering*, vol. 105, no. 3, pp. 645–654, Feb 2010.

[10] C. Potter, S. Schobesberger, M. Lundberg, P. Weinberg, J. Mitchell, and J. Gorelik, "Shape and compliance of endothelial cells after shear stress in vitro or from different aortic regions: scanning ion conductance microscopy study," *PLoS ONE*, vol. 7, no. 5, pp. 1–5, May 2012.

[11] Y.-C. Toh and J. Voldman, "Fluid shear stress primes mouse embryonic stem cells for differentiation in a self-renewing environment via heparan sulfate proteoglycans transduction," *The FASEB Journal*, vol. 25, no. 4, pp. 1208–1217, Apr 2011.

[12] L. Griffith and M. Swartz, "Capturing complex 3d tissue physiology in vitro," *Nature Reviews Molecular Cell Biology*, vol. 7, pp. 211–224, Mar 2006.

[13] J. Culver, J. Hoffmann, R. Poché, J. Slater, J. West, and M. Dickinson, "Three-dimensional biomimetic patterning in hydrogels to guide cellular organization," *Advanced Materials*, vol. 24, no. 17, pp. 2344–2348, May 2012.

[14] M. Song, D. Dean, and M. Knothe Tate, "Mechanical modulation of nascent stem cell lineage commitment in tissue engineering scaffolds," *Biomaterials*, vol. 34, no. 23, pp. 5766–5775, Jul 2013.

[15] P. Tseng and D. Di Carlo, "Substrates with patterned extracellular matrix and subcellular stiffness gradients reveal local biomechanical responses," *Advanced Materials*, vol. 26, no. 8, pp. 1242–1247, Feb 2014.

[16] Z. Zhang, L. Yuan, P. Lee, E. Jones, and J. Jones, "Modeling of time dependent localized flow shear stress and its impact on cellular growth within additive manufactured titanium implants, modeling flow shear and ingrowth in porous implants," *Journal of Biomedical Materials Research. Part B, Applied Biomaterials*, vol. 102, no. 8, pp. 1689–1699, Nov 2014.

[17] R. McCoy, C. Jungreuthmayer, and F. O'Brien, "Influence of flow rate and scaffold pore size on cell behavior during mechanical stimulation in a flow perfusion bioreactor," *Biotechnology and Bioengineering*, vol. 109, no. 6, pp. 1583–1594, Jun 2012.

[18] P. Callaghan, *Principles of nuclear magnetic resonance microscopy*. Clarendon Press Oxford, 1991, vol. 3.

[19] J. Mack, K. Youssef, O. Noel, M. Lake, A. Wu, M. Iruela-Arispe, and L.-S. Bouchard, "Real-time maps of fluid flow fields in porous biomaterials," *Biomaterials*, vol. 34, no. 8, pp. 1980–1986, Mar 2013.

[20] K. Youssef, J. Mack, M. Iruela-Arispe, and L.-S. Bouchard, "Macro-scale topology optimization for controlling internal shear stress in a porous scaffold bioreactor," *Biotechnology and Bioengineering*, vol. 109, no. 7, pp. 1844–1854, Jul 2012.

[21] F. Boschetti, M. Raimondi, F. Migliavacca, and G. Dubini, "Prediction of the micro-fluid dynamic environment imposed to three-dimensional engineered cell systems in bioreactors," *Journal of Biomechanics*, vol. 39, no. 3, pp. 418–425, Jan 2006.

[22] S. Mirbagheri, M. Bagheri, S. Boudaghpour, M. Ehteshami, and Z. Bagheri, "Performance evaluation and modeling of a submerged membrane bioreactor treating combined municipal and industrial wastewater using radial basis function artificial neural networks," *Journal of Environmental Health Science and Engineering*, vol. 13, no. 17, pp. 1–15, 2015.

[23] X. Zhu and X. Ji, "Soft sensing of key state variables in fermentation process based on relevance vector machine with hybrid kernel function," *Sensors and Transducers*, vol. 173, no. 6, pp. 237–243, 2014.

[24] K. Hornik, M. Stinchcombe, and H. White, "Multilayered feedforward networks are universal approximators," *Neural Networks*, vol. 2, no. 5, pp. 359–366, 1989.

[25] E. Rumelhart, G. Hinton, and R. Williams, "Learning representations by back-propagation errors," *Nature*, vol. 323, no. 9, pp. 533–536, 1986.

[26] C.-C. Yu and B.-D. Liu, "A backpropagation algorithm with adaptive learning rate and momentum coefficient," in *Neural Networks, 2002. IJCNN '02. Proceedings of the 2002 International Joint Conference on*, vol. 2, 2002, pp. 1218–1223.

[27] F. Couet, S. Meghezi, and D. Mantovani, "Fetal development, mechanobiology and optimal control processes can improve vascular tissue regeneration in bioreactors: an integrative review," *Medical Engineering & Physics*, vol. 34, no. 3, pp. 269–278, Apr 2012.